Check for updates

Dual anticancer and antibacterial activity of fluorescent naphthoimidazolium salts†

Dung Ngoc Tran, ‡[a] Thi Thuy Hang Hoang, ‡[b] Sondavid Nandanwar,[c] Vuong Thi Thanh Xuan Ho,[d] Van Thong Pham,[e] Huy Duc Vu,[f] Xuan Ha Nguyen,[g] Huy Trung Nguyen,[h] Trang Van Nguyen,[h] Thuy Kieu Van Nguyen,[i] Dai Lam Tran,[h] Myeongkee Park,[j] Songyi Lee [ID] *[ij] and Thanh Chung Pham [ID] *[h]

Cancer has emerged as a significant global health challenge, ranking as the second leading cause of death worldwide. Moreover, cancer patients frequently experience compromised immune systems, rendering them susceptible to bacterial infections. Combining anticancer and antibacterial properties in a single drug could lead to improved overall treatment outcomes and patient well-being. In this context, the present study focused on a series of hydrophilic naphthoimidazolium salts with donor groups (NI-R), aiming to create dual-functional agents with antibacterial and anticancer activities. Among these compounds, NI-TPA demonstrated notable antibacterial activity, particularly against drug-resistant bacteria, with MIC value of 7.8 µg mL^{-1}. Furthermore, NI-TPA exhibited the most potent cytotoxicity against four different cancer cell lines, with an IC$_{50}$ range of 0.67–2.01 µg mL^{-1}. The observed high cytotoxicity of NI-TPA agreed with molecular docking and dynamic simulation studies targeting c-Met kinase protein. Additionally, NI-TPA stood out as the most promising candidate for two-photo excitation, fluorescence bioimaging, and localization in lysosomes. The study findings open new avenues for the design and development of imidazolium salts that could be employed in phototheranostic applications for cancer treatment and bacterial infections.

Introduction

Cancer is a complex and devastating disease characterized by the aberrant proliferation of cells, resulting in the formation of malignant tumors that can infiltrate and disrupt normal body tissues. It arises from genetic mutations in any cell type and can occur in various anatomical locations, leading to its pervasive

[a] *Faculty of Chemistry, Hanoi National University of Education, Hanoi, Vietnam*
[b] *Department of Chemistry, Soongsil University, Seoul 06978, South Korea*
[c] *Eco-friendly New Materials Research Center, Korea Research Institute of Chemical Technology, 141 Gajeong-ro, Yuseong-gu, Daejeon City, Republic of Korea*
[d] *Faculty of Pharmacy, Dong A University, Danang, Vietnam*
[e] *R&D Center, Vietnam Education and Technology Transfer JSC, Cau Giay, Hanoi, Vietnam*
[f] *Department of Radiology, School of Medicine, Daegu Catholic University, Daegu 42472, Korea*
[g] *Institute of Natural Products Chemistry, Vietnam Academy of Science and Technology, 18 Hoang Quoc Viet, Cau Giay, Hanoi, Vietnam*
[h] *Institute for Tropical Technology, Vietnam Academy of Science and Technology, 18 Hoang Quoc Viet, Cau Giay, Hanoi, Vietnam. E-mail: ptchung@itt.vast.vn*
[i] *Industry 4.0 Convergence Bionics Engineering, Pukyong National University, Busan 48513, Korea. E-mail: slee@pknu.ac.kr*
[j] *Department of Chemistry, Pukyong National University, Busan 48513, Korea*

† Electronic supplementary information (ESI) available. See DOI: https://doi.org/10.1039/d3ra06555c

‡ These authors equally contributed to this work.

nature throughout the body.[1–4] As the second-leading cause of mortality worldwide, cancer poses formidable challenges to medical research such as drug resistance and side effects, necessitating continuous efforts in the development of effective drugs and therapies.[5–11] Compounding the burden of cancer and its treatment is the impact on the patient's immune system, rendering patients more susceptible to opportunistic infections, particularly bacterial pathogens. The concomitant presence of multiple diseases further exacerbates the severity of each condition, leading to a challenging clinical scenario.[12–16] Thus, incorporating therapeutic agents with dual functionality, possessing both anti-cancer and antibacterial activities, holds promise in enhancing patient quality of health and life.

The emergence of infectious bacteria poses a growing threat to human health.[17–19] Of particular concern is the prevalence of multi-drug resistance in bacterial strains, exemplified by methicillin-resistant *Staphylococcus aureus* (MRSA), which presents a significant challenge in the management of infectious diseases.[20–22] The development of untreatable bacterial infections is a pressing issue that demands attention in the near future. The molecular design of antibacterial agents encompasses various mechanisms, which can be broadly classified into four categories: inhibition of cell wall synthesis, inhibition of nucleic acid synthesis, and inhibition of protein synthesis, disruption of the cell membrane.[23,24] Among antibacterial

agents, lipophilic complexes have shown promising interactions with the lipophilic layer of bacteria, thereby increasing the membrane permeability of bacteria and subsequent antibacterial activity.[25] Enhancing the lipophilicity of compounds can improve the effectiveness of existing antibacterial drugs currently in clinical use and exploring drug combinations represent potential strategies.

Moreover, recent advances have led to the development of non-invasive diagnostic and therapeutic techniques.[26,27] Notably, the concept of optical biopsy has garnered substantial attention as it fulfills the medical demand for minimally invasive alternatives.[28,29] In this context, optical spectroscopic instruments have been harnessed to transform traditional pathology into real-time spectroscopy in conjunction with biomedical materials. Of particular significance is the emergence of certain chemotherapeutic agents with inherent biocompatible fluorophore properties, such as doxorubicin (DOX), camptothecin, and SN-38.[30,31] Their dual functionality as both therapeutic agents and biocompatible fluorophores makes them valuable tools in the field of medical imaging and targeted therapies.[32–35]

Among therapeutic agents, imidazolium salts have been recognized for antibacterial and/or anticancer activity and their potential biomedicine applications owing to their hydrophilic nature.[36–40] These observations align with our recent research endeavor, which involved the synthesis of a naphthoimidazolium-based fluorescent chemosensor specifically designed for hypochlorite-activated antibacterial activity.[41] Our investigations have revealed that the imidazolium family, encompassing imidazolium, benzimidazolium, and halogenated imidazolium derivatives, has been extensively explored for its antibacterial and anticancer properties.[36–42] However, the exploration of naphthoimidazolium derivatives remains relatively limited.[43,44] Moreover, the past and current design strategies primarily revolve around the introduction of functional groups into the two nitrogen atoms, with little attention given to the examination of the substituent's impact at the carbon position situated between these two nitrogen atoms (Fig. 1).[36–45] Furthermore, it is noteworthy that π-system-expanded imidazolium salts exhibit a redshift in absorption and emission wavelength.[41,43,44,46,47] Our recent inquiry has revealed that **NI-H** and **NI-Cbz** naphthoimidazolium, manifest heightened fluorescence emission in both organic and highly aqueous environments.[47] The photophysical attributes exhibited by naphthoimidazolium render it a promising candidate for applications in fluorescent imaging and phototheranostics.
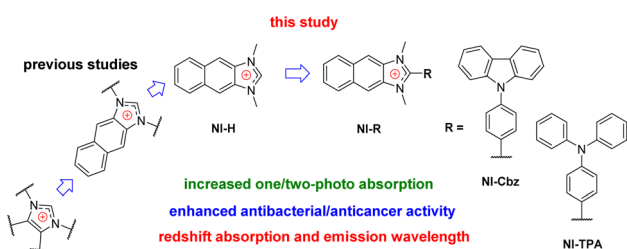
Hence, our investigative efforts continue to involve the synthesis, photophysical examination, theoretical calculation and biological activities of **NI-H** and its derivatives by incorporating donor groups, specifically carbazolyl phenyl and triphenylamine, resulting in **NI-Cbz** and **NI-TPA**, respectively. Among these compounds, **NI-TPA** was evaluated for its potential application in fluorescence bioimaging and lysosome localization using HeLa cells. Moreover, we assessed the antibacterial activity of these compounds against ten bacterial strains, consisting of five Gram-positive and five Gram-negative strains. Furthermore, we explored their anticancer efficacy by studying their cytotoxicity against four different cancer cell lines. Our results revealed that **NI-TPA** exhibited remarkable cytotoxicity against both cancerous cells and bacteria, including MRSA, indicating its potential as a dual-function agent with both anticancer and antibacterial activities. To gain insights into the underlying mechanisms of its anticancer activity, molecular docking, and dynamic simulation were employed to study the interaction between **NI-TPA** and specific proteins in cancer cells.

Results and discussion

Synthetic process and structural characterization

NI-R was synthesized using three key transformations (Scheme 1). The synthesis commenced with the cyclization reaction of 2,3-diaminonaphthalene to form the first intermediate compound (**1-R**). Subsequently, **1-R** underwent methylation by reacting with iodomethane in the presence of sodium hydride in DMF, yielding the second intermediate compound (**2-R**). Finally, the target compound **NI-R** salts were obtained through the refluxing of **2-R** with iodomethane in acetonitrile. The detailed experimental procedures for each step of the synthesis, along with the structural spectra data are documented in the Experimental section and ESI.†

The ¹H NMR spectra of **NI-H** displayed a single peak, characterized by the most prominent chemical shift recorded at 9.85 ppm. This resonance was ascribed to a hydrogen moiety directly bound to a carbon atom positioned intermediary between two nitrogen atoms. Upon the introduction of electron-donating groups at this specific carbon site, the ¹H NMR signal associated with this proton manifestation ceased to manifest.

Fig. 1 Molecular design toward **NI-R**.
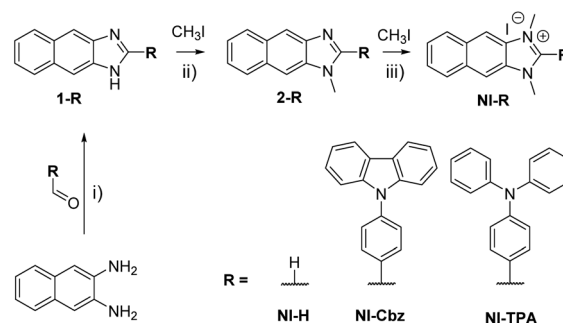
Scheme 1 Synthetic process for **NI-R** structures. (i) DMF, acetic acid, 80 °C, 9 h; (ii) NaH, DMF, argon, RT, 18 h; (iii) CH₃CN, reflux, 12–24 h.

This phenomenon serves as compelling substantiation for the manifestation of conjugative interactions amidst the substituent groups within both the **NI-Cbz** and **NI-TPA** molecular configurations. Furthermore, discernible alterations were discerned in the resonance patterns of the methyl group protons associated with **NI-R**, in contrast to their precursors in the **2-R** configuration. This disparity not only underscores the establishment of said salts but also implies that the proton group equivalency within the **NI-R** construct signifies the liberation of positive charge within the naphthoimidazole framework.

Photophysical properties

In our antecedent report, we undertook an examination of the photophysical properties and theoretical calculations pertaining to **NI-H** and **NI-Cbz**.[47] The investigation into the corresponding attributes of **NI-Cz** is herein expounded. The findings of both analyses have been succinctly compiled and are delineated in Table 1, Fig. 2 and 3.[47] The absorption and fluorescence emission peaks of **NI-H** were observed at 324 nm and 433 nm ($\Phi_F = 0.33$), respectively, in ethanol. The introduction of donor groups into the naphthoimidazolium core resulted in a redshift of the absorption and fluorescence emission peaks. Specifically, **NI-Cbz** exhibited absorption peaks at 335 nm and fluorescence emission peaks at 535 nm, while **NI-TPA** showed absorption peaks at 370 nm and fluorescence emission peaks at 554 nm. Furthermore, the molar absorption coefficients of **NI-H**, **NI-Cbz**,
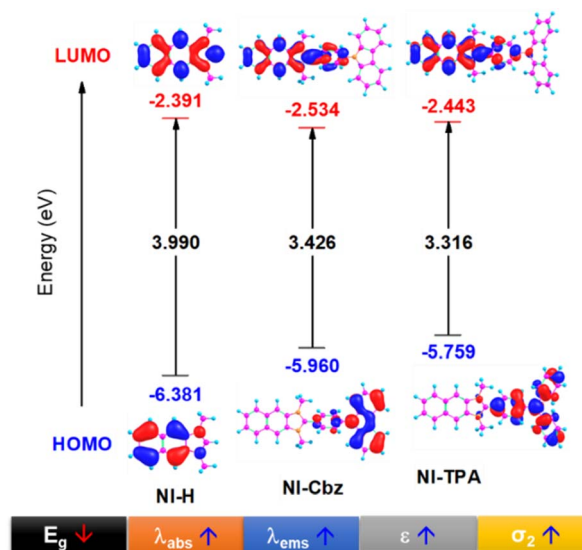
Table 1 Photophysical properties and theoretical calculation results for NI-R structures in ethanol ($^\alpha$in DMSO)^a

	λ_{abs} (nm)	ε (M^{-1} cm^{-1}) ($\times 10^3$)	λ_{ems} (nm)	Φ_F	$\sigma_2{}^\alpha$ (GM)	E_g (eV)
NI-H	324	8.8	433	0.33	11	3.99
NI-Cbz	335	23.6	535	0.04	36	3.43
NI-TPA	370	39.2	554	0.06	75	3.32

^{a} ε (molar absorption coefficient); Φ_F (fluorescence emission quantum yield) was determined utilizing 9,10-diphenylanthracene ($\Phi_F = 0.90$ in cyclohexane) as reference;[46] E_g (energy gap between HOMO and LUMO) was obtained by density functional theory (DFT) calculation using B3LYP/6-31+G(d,p) level of theory in ethanol/PCM solvent model.
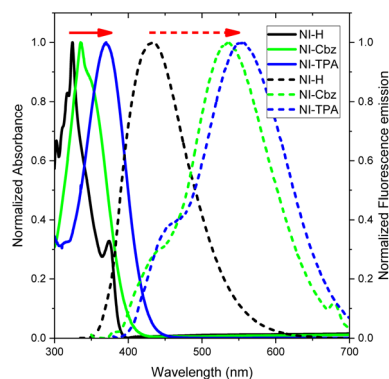

Fig. 2 UV-Vis absorption (solid line) and fluorescence emission spectra (dotted line) of NI-R in ethanol.

Fig. 3 HOMO and LUMO image along with the energy gap (E_g) between HOMO and LUMO of NI-R in ethanol solvent.

and **NI-TPA** were found to increase significantly from 8.8×10^3 to 23.6×10^3 and further to 39.2×10^3 M^{-1} cm^{-1}, respectively. In addition, the augmentation in the TP absorption cross-section (σ_2) denoted by values of 11 GM, 36 GM, and 75 GM at 780 nm for **NI-H**, **NI-Cbz**, and **NI-TPA**, respectively. The redshift in the absorption and fluorescence emission peaks as well as enhanced TP absorbance can be attributed to the enhancement of push–pull effects and intramolecular charge transfer (ICT) resulting from the incorporation of strong donor groups. This is consistent with the observed decrease in the energy gap (E_g) between LUMO and HOMO from 3.99 to 3.43 and then 3.32 eV. Moreover, molecular orbital (MO) analysis revealed that the HOMO and LUMO of **NI-H** were in the naphthoimidazolium core (Fig. 3). Conversely, for **NI-Cbz** and **NI-TPA**, the HOMO was mainly localized in the carbazolyl phenyl and triphenylamine groups, respectively, while the LUMO remained primarily situated in the naphthoimidazolium core. This confirms the presence of a donor–acceptor framework in the structures of **NI-Cbz** and **NI-TPA**. Additionally, the fluorescence emission quantum yields (Φ_F) of **NI-Cbz** and **NI-TPA** were calculated to be 0.04 and 0.06, respectively. Overall, based on the observed photophysical properties including absorption and emission wavelength, molar absorption coefficients, and fluorescence, **NI-TPA** demonstrated the most promising potential for fluorescence bioimaging among the three **NI-R** salts studied.

Fluorescence imaging in living cell

Motivated by the fluorescence emission of **NI-TPA** in both organic and aqueous solvents, the present research investigates its potential as a fluorescence agent for live-cell imaging, employing confocal laser scanning microscopy (CLSM). This study involves the examination of the cellular uptake efficiency of **NI-TPA** in HeLa cells after a 30 minute incubation period. Fig. 4a displays a remarkable fluorescent emission within the
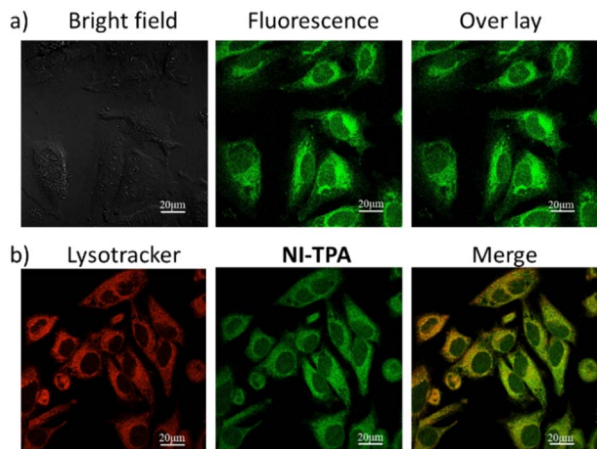
Fig. 4 CLSM image of HeLa cells (a) after incubation with **NI-TPA** (10 μM), (b) after co-incubation of **NI-TPA** (10 μM) with Lysotracker Red (50 nM).

HeLa cells, indicating a rapid internalization of the **NI-TPA**. This notable fluorescence capability in living cells can be attributed to **NI-TPA**'s ability to emit fluorescence across a wide range of solvent environments. In addition, **NI-TPA** shows a high TP absorption cross-section ($\sigma_2 = 75$ GM) that holds significant advantageous implications for the field of near infrared (NIR) light-excited fluorescence bioimaging through two-photon excitation technique.

To gain further insights into the selective localization of **NI-TPA** within specific cellular organelles, colocalization experiments were conducted. Specifically, HeLa cells were co-stained with **NI-TPA** and Lysotracker Red. Fig. 4b demonstrates the tendency of **NI-TPA** to localize in lysosomes, showing a high Pearson correlation coefficient of 0.78. Lysosomes are membrane-bound organelles responsible for vital cellular processes such as degradation and recycling of cellular waste, cellular signalling, and energy metabolism.[48] Thus, **NI-TPA** shows promise as a potential lysosome-targeted fluorescent drug for cancer chemotherapy.

Antibacterial activity test

Table 2 provides a comprehensive summary of MICs observed for the **NI-R** series, elucidating their antibacterial activity. Notably, naphthoimidazolium salt (**NI-H**) did not exhibit growth inhibition against the tested bacteria. However, the introduction of carbazolyl phenyl and triphenylamine groups significantly enhanced the antibacterial activity of naphthoimidazolium salt against Gram-positive bacteria, such as MRSA, *S. aureus*, and *L. monocytogenes*, with MIC values ranging from 2 to 16 μg mL^{-1} (Table 2). In particular, **NI-TPA** demonstrated higher antibacterial activity against MRSA and *S. aureus* compared to **NI-Cbz**. Conversely, **NI-Cbz** exhibited stronger antibacterial activity against *L. monocytogenes* in comparison to **NI-TPA**. The augmented growth inhibition of **NI-Cbz** and **NI-TPA** against Gram-positive bacteria can be attributed to the electrostatic interaction between the positively charged salt and the negatively charged bacterial cell membrane. This electro-static interaction mechanism may explain the non-antibacterial

Table 2 Minimal inhibitory concentration (MIC) (μg mL^{-1}) of **NI-R** compounds against various bacterial strains: MRSA (1), *S. aureus* (2), *B. subtilis* (3), *E. faecalis* (4), *L. monocytogenes* (5), ESBL (6), *E. coli* (7), *S. typhimurium* (8), *K. pneumoniae* (9), and *V. parahaemolyticus* (10) (— MIC > 250 μg mL^{-1})

Bacteria		NI-H	NI-Cbz	NI-TPA
Gram-positive	1	—	16 ± 0.004	7.8 ± 0.003
	2	—	7.8 ± 0.002	3.9 ± 0.001
	3	—	—	—
	4	—	—	—
	5	—	2 ± 0.001	3.9 ± 0.001
Gram-negative	6	—	—	—
	7	—	—	—
	8	—	7.8 ± 0.003	7.8 ± 0.002
	9	—	—	—
	10	—	—	—

activity of both compounds against nearly all Gram-negative bacteria, as evidenced in Table 2. However, they did exhibit growth inhibition against *S. typhimurium*. It is worth noting that the cell walls of Gram-positive and Gram-negative bacteria exhibit distinct structural characteristics. Gram-positive bacteria possess a multilayered composition of peptidoglycan and teichoic acids within their cell walls. In contrast, Gram-negative bacteria possess a relatively thinner cell wall comprising a limited number of peptidoglycan layers, which is further enveloped by an outer lipid membrane consisting of lipopolysaccharides and lipoproteins. Consequently, the susceptibility of different compounds toward Gram-positive and Gram-negative bacteria may vary due to these structural disparities.[49,50]

In summary, **NI-TPA** demonstrated the strongest growth inhibition against *S. aureus* and MRSA, with MIC values of approximately 3.9 μg mL^{-1} and 7.8 μg mL^{-1}, respectively. In addition, **NI-Cbz** exhibited the highest antibacterial activity against *L. monocytogenes*, with a MIC value of approximately 2 μg mL^{-1}. Both **NI-Cbz** and **NI-TPA** exhibited similar antibacterial activity against *S. typhimurium*, with a MIC value of approximately 7.8 μg mL^{-1}. These MIC values show a low range in the comparison with those reported in the existing literature for imidazolium salts.[12,37,38,45] Hence, **NI-Cbz** and **NI-TPA** possess the potential to serve as promising therapeutic agents for the treatment of various infections, including drug-resistant bacterial strains.

Anticancer activity test

The antibacterial properties of **NI-Cbz** and **NI-TPA** compounds have demonstrated efficacy against both Gram-positive and Gram-negative bacterial strains, which has inspired us to investigate their cytotoxic effects on four distinct cancer cell lines: MCF7, A549, HepG2, and HeLa. Our initial analysis revealed that the **NI-H** control structure displayed anticancer activity, with an IC$_{50}$ range of 9.03–18.40 μg mL^{-1}. Subsequently, the introduction of a carbazolyl phenyl group in **NI-Cbz** resulted in enhanced cytotoxicity towards MCF7 and HepG2 cells, with IC$_{50}$ values of 1.76 and 1.45 μg L^{-1}, respectively. However, **NI-Cbz** exhibited low cytotoxicity towards HeLa cells

Table 3 IC$_{50}$ (µg mL^{-1}) of NI-R salts

	NI-H	NI-Cbz	NI-TPA	Ellipticine
MCF7	18.40 ± 0.77	1.76 ± 0.07	0.67 ± 0.03	0.39 ± 0.02
A549	6.92 ± 0.42	>100	1.07 ± 0.08	0.46 ± 0.03
HepG2	9.38 ± 0.43	1.45 ± 0.12	**0.31 ± 0.03**	0.35 ± 0.01
HeLa	9.03 ± 0.37	36.11 ± 0.73	2.01 ± 0.15	0.44 ± 0.03

(IC$_{50}$ = 36.11 µg mL^{-1}) and negligible cytotoxicity towards A549 cells (IC$_{50}$ > 100 µg mL^{-1}).

Significantly, the incorporation of the triphenylamine moiety into **NI-H** results in the generation of the **NI-TPA** product, manifesting pronounced improvements in cytotoxic efficacy against a spectrum of four distinct cancer cell lines, with IC$_{50}$ values ranging from 0.31 to 2.01 µg mL^{-1}. Notably, the IC$_{50}$ value of **NI-TPA** was the lowest among the three products tested. The IC$_{50}$ of **NI-TPA** against HepG2 cells was lowest among four cancer cell lines (Table 3). These findings underscore the potential application of **NI-TPA** as an effective anticancer drug. Given the promising cytotoxicity of **NI-TPA**, we further investigated the interaction mechanism between **NI-TPA** and HepG2 cells using MD simulations. This computational approach will provide valuable insights into the molecular-level interactions between **NI-TPA** and cancer cells, elucidating the underlying mechanisms of its potent anticancer activity.

Molecular docking and dynamics analysis

The geometric structure of **NI-R** was optimized utilizing Density Functional Theory (DFT) calculations at the B3LYP/6-31+G(d,p) level of theory within the Gaussian 16 program. The architectural arrangements of **NI-R** structures exhibited a consistent configuration within the naphthoimidazolium core. Notably,

both **NI-Cbz** and **NI-TPA** displayed highly identical rotation angles between donor groups and the naphthoimidazolium core, as depicted in Fig. S3.† Consequently, the introduction of electron-donating groups was observed to enhance the anti-bacterial and anticancer activities of the compounds. Furthermore, it was observed that the diphenyl amino group exhibited a greater affinity towards cancer cells in comparison to the carbazole group. To gain a more profound insight into the mechanisms underlying the action of **NI-R** structures, molecular docking simulations were conducted. These simulations aimed to elucidate the potential anticancer properties of **NI-R** salts the protein c-Met kinase,[51,52] which is one of the pathways in human cancer that is dysregulated most commonly. Tumor angiogenesis, metastasis, and tumor cell proliferation, survival, migration, and invasion are all facilitated by an active c-Met signaling system.[53] Inhibiting c-Met kinase can help control the growth of many human malignancies, making c-Met kinase inhibitors a valuable approach in cancer therapy.[54] Consequently, c-Met has drawn a lot of interest as a possible target for therapeutic intervention in oncology.

Initially, the co-crystallized ARQ 197 ligand was re-docked into the catalytic domain of c-Met kinase using AutoDock Vina v1.2.0 (ref. 55) to validate the docking protocol. The results of the ARQ 197 ligand redocking revealed a RMSD value of 0.362 Å, indicating a precise co-crystallized ligand's binding conformation prediction. After that, **NI-H**, **NI-Cbz**, and **NI-TPA** were docked into the binding pocket of the c-Met kinase protein. Interestingly, the docking results of these compounds exhibited favorable affinities towards the c-Met kinase protein, as demonstrated by their high binding energies of −8.646, −10.490, and −11.03 kcal mol^{-1} for **NI-H**, **NI-Cbz**, and **NI-TPA**, respectively. The evaluation of **NI-H** compounds' interaction capabilities with the active site of c-Met kinase revealed the
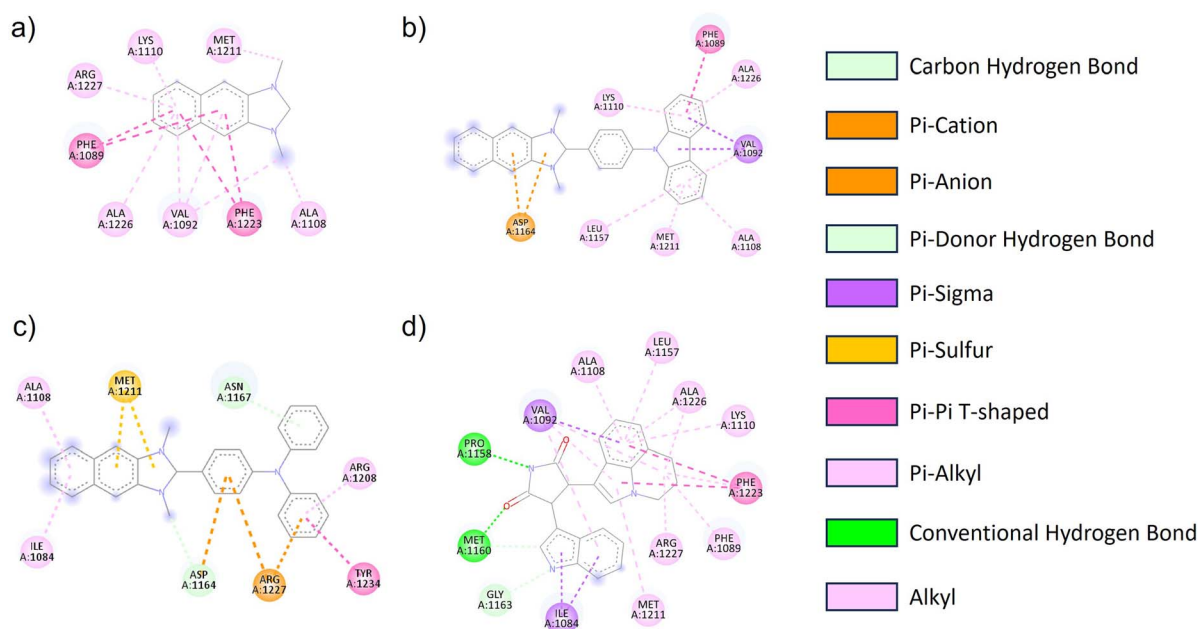

Fig. 5 2D diagrams of the interactions between the (a) NI-H, (b) NI-Cbz, (c) NI-TPA, (d) erlotinib and residues in the c-Met kinase receptor.

Table 4 Binding energies and interactions of the protein c-Met kinase–ligand complex

	Binding energy (kcal mol^{-1})	Type of interaction	Amino acid residues
NI-H	−8.646	Pi–alkyl and alkyl	Arg1227, Lys1110, Met1211, Ala1226, Val1092, Ala1108
		Pi–pi stacked	Phe1089, Phe1223
NI-Cbz	−10.49	Pi–alkyl	Lys1110, Ala1226, Leu1157, Met1211, Ala1108
		Pi–pi stacked	Phe1089
		Pi–sigma	Val1092
		Pi–anion	Asp1164
NI-TPA	−11.03	Pi–alkyl	Ala1108, Ile1084, Arg1208
		Pi–pi T-shaped	Tyr1234
		Pi–ion	Arg1227, Asp1164
		Pi–sulfur	Met1211
ARQ 197	−13.24	Pi–alkyl and alkyl	Ala1108, Leu1157, Ala1226, Lys1110, Arg1227, Phe1089, Met1211
		Pi–sigma	Val1092, Ile1084
		Pi–pi T-shaped	Phe1223
		Hydrogen bond	Pro1158, Met1160
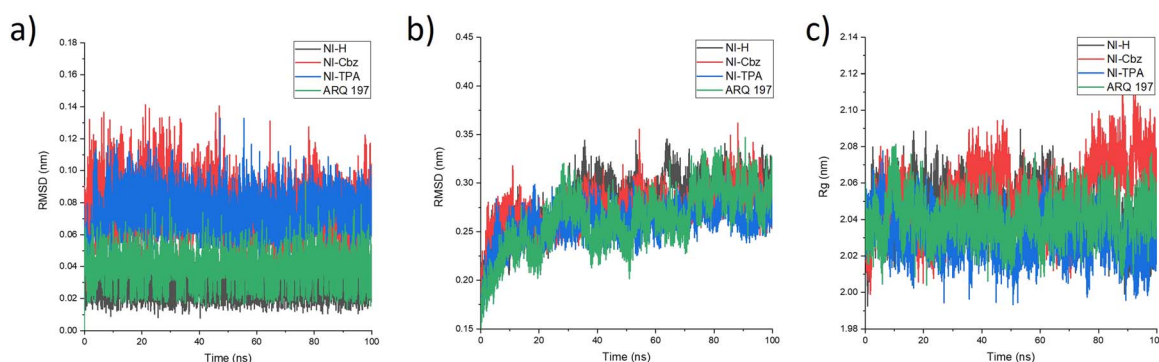
Fig. 6 (a) RMSD of the backbone protein, (b) RMSD of the ligand, and (c) R_g analysis for the MD simulations.

formation of six pi–alkyl and alkyl interactions with Arg1227, Lys1110, Met1211, Ala1226, Val1092, and Ala1108, along with two pi–sigma interactions with Phe1089 and Phe1223 (Fig. 5 and Table 4). Meanwhile, **NI-Cbz** forms pi–alkyl, pi–pi T-shaped, and pi–sigma interactions focused on a carbazole group with amino acid residues, namely Lys1110, Ala1226, Leu1157, Met1211, Ala1108 (pi–alkyl interactions), Phe1089 (pi–pi T-shaped interaction) and Val1092 (pi–sigma interaction). Regarding **NI-TPA**, this compound formed pi–alkyl, pi–sulfur, pi–pi T-shaped, and pi–ion interactions. Namely, it engages in pi–alkyl interaction with residues Ala1108, Ile1084, Arg1208, pi–sulfur interaction with residue Met1211 and pi–ion interaction with Arg1227 and Asp1164 (Fig. 5). The results on binding energies and interactions between ligands and c-Met kinase protein show that **NI-TPA** ligand binds better with c-Met kinase protein. These findings are consistent with the *in vitro* experimental results, where **NI-TPA** exhibits the lowest IC$_{50}$ compared to **NI-H** and **NI-Cbz** (Table 3).

To further evaluate the stability of the complexes, the RMSD and R_g were calculated for all the saved structures during the MD simulation, and the changes in these factors were measured and are illustrated in Fig. 6. The RMSD of the c-Met kinase protein remains below 3 Å throughout the simulation, indicating its stable structure. The average RMSD values of the c-Met kinase protein in complex with **NI-H**, **NI-Cbz**, **NI-TPA**, and

ARQ 197 are 0.280, 0.271, 0.258, and 0.261 nm, respectively while the average RMSD values of **NI-H**, **NI-Cbz**, **NI-TPA**, and ARQ 197 in complex with c-Met kinase protein is 0.029, 0.076, 0.074, and 0.037 nm, respectively. All the results are below 0.3 nm[56] indicate the stability of **NI-H**, **NI-Cbz**, **NI-TPA**, and ARQ 197 in the active site of the c-Met kinase protein during the simulation. The R_g was used to assess the compactness of the protein during the simulation. The R_g values of the c-Met kinase protein in all complexes fall within a narrow range of 1.90–2.02 nm and do not show any abnormal changes during the simulation. The average R_g values of c-Met kinase protein is 2.044, 2.053, 2.030, and 2.041 nm in the complexes with the c-Met kinase protein bound to **NI-H**, **NI-Cbz**, **NI-TPA**, and ARQ 197. The RMSD and R_g results indicate that throughout the simulation, ligands stably bound and didn't leave the active site of the target protein and the whole system was in a relaxed conformation.[57]

Conclusion

We synthesized a hydrophilic naphthoimidazolium salt (**NI-H**) and its derivatives, namely **NI-Cbz** and **NI-TPA**, by incorporating donor groups. The introduction of these donor groups resulted in redshifts of both the UV-Vis absorption and fluorescence emission peaks along with TP absorption cross-section from **NI-H** to **NI-Cbz** and further to **NI-TPA**. Importantly, **NI-TPA**

demonstrated fluorescence emission and lysosome localization after incubation with HeLa cells, indicating its potential as a promising agent for fluorescence bioimaging applications. Furthermore, **NI-Cbz** and **NI-TPA** exhibited the antibacterial activity against three Gram-positive bacteria (*L. monocytogenes*, *S. aureus*, and MRSA) and one Gram-negative bacterium (*S. typhimurium*). Notably, **NI-Cbz** showed MIC of 2 μg mL^{-1} against *L. monocytogenes*, while **NI-TPA** displayed the lowest MIC (3.9 μg mL^{-1}) against both *L. monocytogenes* and *S. aureus*. These findings underscore the potential of these naphthoimidazolium derivatives as antibacterial agents, particularly **NI-TPA**. Additionally, we investigated the cytotoxicity of **NI-H**, **NI-Cbz**, and **NI-TPA** against four different cancer cell lines (MCF7, A549, HepG2, and HeLa). Among these structures, **NI-TPA** demonstrated the highest cytotoxicity, with IC$_{50}$ values ranging from 0.67–2.01 μg mL^{-1}, further highlighting its potent anticancer activity. Molecular interactions between **NI-R** salts and c-Met kinase protein in cancer cells were also explored by docking and MD simulation, shedding light on the underlying mechanisms of their anticancer properties. In conclusion, the incorporation of donor groups, particularly the triphenylamine group, into the naphthoimidazolium salt led to enhanced one-photon absorption, emission wavelengths and TP absorption cross section, as well as improved antibacterial and anticancer activities. This study presents a novel design of imidazolium salts with promising potential for phototheranostic applications in cancer treatment and bacterial infections.

Experimental

Synthetic process

NI-R was synthesized using a three-step process starting from 2,3-diaminonaphthalene as the initial material. Previously reported procedures were employed to prepare **NI-H** and **NI-Cbz**.[47] The synthesis of **NI-TPA** is detailed below.

Synthesis of 1-TPA. In a 30 mL solution of dimethylformamide (DMF), 2,3-diaminonaphthalene (1.0 mmol) and 4-(diphenylamino)benzaldehyde (1.1 equivalent) were stirred together in the presence of acetic acid (0.1 mL) at 90 °C for 8 hours. Subsequently, the reaction mixture was transferred to 50 mL of deionized water. The organic crude product was collected by extracting the mixture three times with 100 mL of methylene chloride (MC). After drying the organic phase with anhydrous Na$_2$SO$_4$, the solvent was removed by evaporation, yielding a crude product. The purification of the crude product was achieved through column chromatography using a mixture of MC and methanol (MeOH) in a ratio of 98 : 2 as the eluent, resulting in the isolation of a white powder of the desired product (yield 45%). ^{1}H NMR (400 MHz, chloroform-*d*) δ 8.81 (s, 2H), 8.07 (ddd, *J* = 8.4, 6.8, 1.5 Hz, 4H), 7.70 (ddd, *J* = 8.4, 6.6, 1.6 Hz, 2H), 7.67–7.58 (m, 8H), 7.21–7.14 (m, 4H).

Synthesis of 2-TPA. To a 20 mL solution of DMF, a mixture of **1-TPA** (1.0 mmol) and iodomethane (2.0 equivalent) was stirred at 0 °C for 15 minutes. Sodium hydride (NaH) (0. equivalent) was then added to the mixture, and stirring was continued at room temperature for 18 hours. The reaction mixture was dissolved in 20 mL of DW and extracted with 100 mL of MC three

times. The organic phase was dried with anhydrous Na$_2$SO$_4$ and concentrated by evaporation. Purification of the crude product was accomplished by column chromatography using a mixture of MC and MeOH (98 : 2) as the eluent, leading to the isolation of a white powder of the desired product (yield 50%). ^{1}H NMR (400 MHz, chloroform-*d*) δ 8.23 (d, *J* = 1.1 Hz, 1H), 8.03–7.96 (m, 1H), 7.96–7.90 (m, 1H), 7.73–7.66 (m, 3H), 7.45–7.35 (m, 2H), 7.35–7.26 (m, 4H), 7.21–7.14 (m, 6H), 7.14–7.05 (m, 2H), 3.93 (s, 3H).

Synthesis of NI-TPA. A mixture of **2-TPA** (1.0 mmol) and iodomethane (1.5 equivalent) was refluxed in 20 mL of acetonitrile for 24 hours. The reaction mixture was then allowed to cool to room temperature, concentrated by evaporation, and dissolved in 2 mL of MeOH. Next, 50 mL of hexane was added to the mixture. The resulting precipitate was isolated through filtration and subsequently washed with 200 mL of hexane, yielding a white powder as desired product (yield 85%): ^{1}H NMR (400 MHz, DMSO-*d*$_6$) δ 8.65 (s, 2H), 8.22 (dt, *J* = 6.6, 3.3 Hz, 2H), 7.81–7.73 (m, 2H), 7.68 (dt, *J* = 6.5, 3.2 Hz, 2H), 7.52–7.43 (m, 4H), 7.34–7.24 (m, 6H), 7.10–7.02 (m, 2H), 4.01 (s, 6H); ^{13}C NMR (101 MHz, DMSO-*d*$_6$) δ 155.01, 151.96, 145.91, 132.93, 131.77, 131.58, 130.73, 128.77, 127.08, 126.98, 126.27, 118.63, 110.78, 33.66; ESI HRMS *m/z* = 440.2125 [M]$^+$, calc. for C$_{31}$H$_{26}$N$_3$ = 440.21.

Antibacterial activity tests

We aimed to assess the antibacterial properties of **NP-R** against a panel of diverse bacterial strains, encompassing both Gram-positive and Gram-negative bacteria. The Gram-positive strains that were investigated included Methicillin Resistant *Staphylococcus aureus* (MRSA), *Staphylococcus aureus* (*S. aureus*), *Bacillus subtilis* (*B. subtilis*), *Enterococcus faecalis* (*E. faecalis*), and *Listeria monocytogenes* (*L. monocytogenes*). The Gram-negative strains tested in this study comprised Extended Spectrum Beta-Lactamase (ESBL), *Escherichia coli* (*E. coli*), *Salmonella typhimurium* (*S. typhimurium*), *Klebsiella pneumoniae* (*K. pneumoniae*), and *Vibrio parahaemolyticus* (*V. parahaemolyticus*). To assess the effectiveness of **NP-R** against these bacterial strains, we determined the Minimal Inhibitory Concentration (MIC) following protocol outlined in our previous report.[23]

Anticancer activity tests

The investigation into anticancer activity was conducted at the Institute of Biological Technology, Vietnam Academy of Science and Technology. This study aimed to evaluate the *in vitro* cytotoxicity of the **NP-R** series on four different cancer cell lines: MCF7 (human breast carcinoma), A549 (hepatocellular carcinoma), HepG2 (human liver carcinoma) and HeLa (human cervical carcinoma). The determination of the half maximal inhibitory concentration (IC$_{50}$) and the subsequent detailed cell experiments were performed following our previous publication.[58]

Molecular dynamic simulation

The anticancer potential of **NI-R** salts was subjected to further screening for molecular docking analysis to examine their

binding modes and suppression against the human mesenchymal–epithelial transition factor (c-Met) protein (PDB ID 3RHK).[59] The crystal structure of the c-Met kinase protein co-crystallized with ARQ 197 (ref. 60) ligand was downloaded from the RCSB Protein Data Bank (https://www.rcsb.org/structure/3RHK). Using PyMOL v2.5 software,[61] water molecules, and ARQ 197 ligand were eliminated from the c-Met macromolecule. Hydrogen atoms in the protein structure were added, and Kollman charges were calculated using AutoDockTools (ADT). To prepare the input for docking simulations, the PDB structure file was converted to PDBQT format. A grid box of dimensions $24 \times 24 \times 24$ Å^3 was generated around the active site of the c-Met kinase protein with a spacing of 1 Å, assisted by ADT. The center of the grid box was set at the center of the c-Met kinase–Erlotinib complex. During the docking process, the c-Met kinase protein was kept rigid, while **NI-H**, **NI-Cbz**, and **NI-TPA** were set to be flexible. ADT and the AutoDock Vina v1.2.0 package were utilized for the molecular docking process.[62] To evaluate the binding energies of the inhibitory complexes produced by **NI-H**, **NI-Cbz**, and **NI-TPA** with the c-Met kinase and to study their interaction potential, the output findings were examined using Discovery Studio Visualizer software. These complexes were then further characterized by molecular dynamics (MD). GROMACS v2022.5 package was used to simulate the molecular dynamics of the protein–ligand complexes.[63] The force field for proteins was chosen to be the AMBER-f99SB-ILDN forcefield, and the Swissparam server created the ligand topologies.[64] TIP3P water molecules were used in a rectangular box to dissolve all of the compounds.[65] The necessary quantity of Na$^+$ and Cl$^-$ ions was introduced, together with salt concentrations of 0.15 mol L^{-1} in each system, to make the simulation system electrically neutral. All the solvated systems underwent 50 000 steps of energy minimization using the steepest descent method. The production run, NVT, and NPT equilibrations were then performed in the MD simulation. These equilibrations were carried out for a total of 300 ps at a temperature of 300 K and a pressure of 1 atm. In the simulation, the V-rescale thermostat and the C-rescale barostat were chosen. Finally, an MD simulation run of 100 ns was carried out. After that, a comparison analysis was done to evaluate the stability of the complexes by measuring the root mean square deviation (RMSD) and the radius of gyration (R_g).

Author contributions

N. D. T. and T. H. N. synthesized structures, T. T. H. H. and H. D. V. performed cell experiments, S. N. and V. T. T X. H. conducted bacterial experiments, V. T. P. and X. H. N. prepared molecular docking and dynamic simulation, V. T. N. and T. K. V. N. performed DFT calculation, M. P. measured TP absorption, D. L. T. and S. L. analysed NMR, T. C. P. prepared manuscript.

Conflicts of interest

There are no conflicts to declare.

Acknowledgements

Notes and references

1 M. Labrie, J. S. Brugge, G. B. Mills and I. K. Zervantonakis, *Nat. Rev. Cancer*, 2022, **22**, 323–339.

2 Y. Cheng, L. Zhao, Y. Li and T. Xu, *Chem. Soc. Rev.*, 2011, **40**, 2673–2703.

3 L. Wang, L. Lankhorst and R. Bernards, *Nat. Rev. Cancer*, 2022, **22**, 340–355.

4 K. Engle and G. Kumar, *Eur. J. Med. Chem.*, 2022, **239**, 114542.

5 Y. Lu, X. Ma, X. Chang, Z. Liang, L. Lv, M. Shan, Q. Lu, Z. Wen, R. Gust and W. Liu, *Chem. Soc. Rev.*, 2022, **51**, 5518–5556.

6 S. M. Meier-Menches, C. Gerner, W. Berger, C. G. Hartinger and B. K. Keppler, *Chem. Soc. Rev.*, 2018, **47**, 909–928.

7 T. Zou, C. T. Lum, C.-N. Lok, J.-J. Zhang and C.-M. Che, *Chem. Soc. Rev.*, 2015, **44**, 8786–8801.

8 M. Tilaoui, H. Ait Mouse and A. Zyad, *Front. Pharmacol*, 2021, **12**, 719694.

9 C. Santini, M. Pellei, V. Gandin, M. Porchia, F. Tisato and C. Marzano, *Chem. Rev.*, 2014, **114**, 815–862.

10 T. C. Johnstone, K. Suntharalingam and S. J. Lippard, *Chem. Rev.*, 2016, **116**, 3436–3486.

11 S. H. Hassanpour and M. Dehghani, *J. Cancer Res. Pract.*, 2017, **4**, 127–129.

12 D. Osmaniye, B. N. Sağlık, N. Khalilova, S. Levent, G. Bayazıt, Ü. D. Gül, Y. Özkay and Z. A. Kaplancıklı, *ACS Omega*, 2023, **8**, 6669–6678.

13 M. R. Felício, O. N. Silva, S. Gonçalves, N. C. Santos and O. L. Franco, *Front. Chem.*, 2017, **5**, 5.

14 A. F. Mohamed, M. Nasr, M. E. Amer, T. M. M. Abuamara, W. M. Abd-Elhay, H. F. Kaabo, E. E. R. Matar, L. E. El Moselhy, T. A. Gomah, M. A. E. L. F. Deban and R. I. Shebl, *Infect. Agents Cancer*, 2022, **17**, 4.

15 Y. Li, P. S. Kumar, S. Tan, C. Huang, Z. Xiang, X. Qiu, X. Tan, J. Luo and M. He, *RSC Adv.*, 2022, **12**, 24130–24138.

16 B. Pucelik, A. Sułek, M. Borkowski, A. Barzowska, M. Kobielusz and J. M. Dąbrowski, *ACS Appl. Mater. Interfaces*, 2022, **14**, 14981–14996.

17 C. Barton Behravesh, T. F. Jones, D. J. Vugia, C. Long, R. Marcus, K. Smith, S. Thomas, S. Zansky, K. E. Fullerton, O. L. Henao, E. Scallan and G. FoodNet Working, *J. Infect. Dis.*, 2011, **204**, 263–267.

18 D. Han, X. Liu and S. Wu, *Chem. Soc. Rev.*, 2022, **51**, 7138–7169.

19 W. Li, F. Separovic, N. M. O'Brien-Simpson and J. D. Wade, *Chem. Soc. Rev.*, 2021, **50**, 4932–4973.

20 S. Sethupathy, L. Vigneshwari, A. Valliammai, K. Balamurugan and S. K. Pandian, *RSC Adv.*, 2017, **7**, 23392–23406.

21 S. Gowrishankar, A. Kamaladevi, K. S. Ayyanar, K. Balamurugan and S. K. Pandian, *RSC Adv.*, 2015, **5**, 95788–95804.

22 J. Xi, L. An, G. Wei, Y. Huang, D. Li, L. Fan and L. Gao, *Biomater. Sci.*, 2020, **8**, 6225–6234.

23 S. K. Nandanwar, S. B. Borkar, B. N. Wijaya, J. H. Cho, N. H. Tarte and H. Jun Kim, *ChemistrySelect*, 2020, **5**, 3471–3476.

24 S. K. Nandanwar and H. J. Kim, *ChemistrySelect*, 2019, **4**, 1706–1721.

25 A. M. Abu-Dief and I. M. A. Mohamed, *Beni-Suef Univ. J. Basic Appl. Sci.*, 2015, **4**, 119–133.

26 Z. Xie, T. Fan, J. An, W. Choi, Y. Duo, Y. Ge, B. Zhang, G. Nie, N. Xie, T. Zheng, Y. Chen, H. Zhang and J. S. Kim, *Chem. Soc. Rev.*, 2020, **49**, 8065–8087.

27 V.-N. Nguyen, Z. Zhao, B. Z. Tang and J. Yoon, *Chem. Soc. Rev.*, 2022, **51**, 3324–3340.

28 N. S. H. Motlagh, P. Parvin, F. Ghasemi and F. Atyabi, *Biomed. Opt. Express*, 2016, **7**, 2400–2406.

29 I. J. Bigio and S. G. Bown, *Cancer Biol. Ther.*, 2004, **3**, 259–267.

30 C. Hu, S. Xu, Z. Song, H. Li and H. Liu, *Chemosensors*, 2023, **11**, 125.

31 M. L. Kabir, F. Wang and A. H. A. Clayton, *Biology*, 2022, **11**, 1135.

32 J. Han, M. Won, J. H. Kim, E. Jung, K. Min, P. Jangili and J. S. Kim, *Chem. Soc. Rev.*, 2020, **49**, 7856–7878.

33 J. H. Kim, P. Verwilst, M. Won, J. Lee, J. L. Sessler, J. Han and J. S. Kim, *J. Am. Chem. Soc.*, 2021, **143**, 14115–14124.

34 A. Sharma, M.-G. Lee, M. Won, S. Koo, J. F. Arambula, J. L. Sessler, S.-G. Chi and J. S. Kim, *J. Am. Chem. Soc.*, 2019, **141**, 15611–15618.

35 C.-H. Whang, E. Yoo, S. K. Hur, K. S. Kim, D. Kim and S. Jo, *Chem. Commun.*, 2018, **54**, 9031–9034.

36 J.-L. Yang, Y.-H. Ma, Y.-H. Li, Y.-P. Zhang, H.-C. Tian, Y.-C. Huang, Y. Li, W. Chen and L.-J. Yang, *ACS Omega*, 2019, **4**, 20381–20393.

37 P. Ganapathi, K. Ganesan, M. Dharmasivam, M. M. Alam and A. Mohammed, *ACS Omega*, 2022, **7**, 44458–44469.

38 L. A. Ismail, R. Zakaria, E. M. Hassan, M. Y. Alfaifi, A. A. Shati, S. E. I. Elbehairi, A. A. El-Bindary and R. F. M. Elshaarawy, *RSC Adv.*, 2022, **12**, 28364–28375.

39 G. Deng, B. Zhou, J. Wang, Z. Chen, L. Gong, Y. Gong, D. Wu, Y. Li, H. Zhang and X. Yang, *Eur. J. Med. Chem.*, 2019, **168**, 232–252.

40 B. D. Wright, M. C. Deblock, P. O. Wagers, E. Duah, N. K. Robishaw, K. L. Shelton, M. R. Southerland, M. A. DeBord, K. M. Kersten, L. J. McDonald, J. A. Stiel, M. J. Panzner, C. A. Tessier, S. Paruchuri and W. J. Youngs, *Med. Chem. Res.*, 2015, **24**, 2838–2861.

41 T. C. Pham, V.-N. Nguyen, Y. Choi, D. Kim, O.-S. Jung, D. J. Lee, H. J. Kim, M. W. Lee, J. Yoon, H. M. Kim and S. Lee, *Front. Chem.*, 2021, **9**, 713078.

42 L.-X. Liu, X.-Q. Wang, B. Zhou, L.-J. Yang, Y. Li, H.-B. Zhang and X.-D. Yang, *Sci. Rep.*, 2015, **5**, 13101.

43 N. Kwon, G. Baek, K. M. K. Swamy, M. Lee, Q. Xu, Y. Kim, S.-J. Kim and J. Yoon, *Dyes Pigm.*, 2019, **171**, 107679.

44 X. Zhang, G. Ko, J. F. Joung, M. Li, Y. Jeong, K. M. K. Swamy, D. Lee, Y. Liu, S. Lee, S. Park, T. D. James and J. Yoon, *Chem. Commun.*, 2018, **54**, 13264–13267.

45 S. N. Riduan and Y. Zhang, *Chem. Soc. Rev.*, 2013, **42**, 9055–9070.

46 T. C. Pham, D. J. Lee, D. H. Kim, J. Yoon, T. D. Lam, H. M. Kim and S. Lee, *Chem. Commun.*, 2023, **59**, 4503–4506.

47 T. C. Pham, T. T. H. Hoang, D. N. Tran, G. Kim, T. V. Nguyen, T. V. Pham, S. Nandanwar, D. L. Tran, M. Park and S. Lee, *ACS Appl. Mater. Interfaces*, 2023, **15**, 47969–47977.

48 S. R. Bonam, F. Wang and S. Muller, *Nat. Rev. Drug Discovery*, 2019, **18**, 923–948.

49 P. O. Asekunowo, R. A. Haque, M. R. Razali and S. Budagumpi, *Appl. Organomet. Chem.*, 2015, **29**, 126–137.

50 A. A. El-Sherif, *J. Solution Chem.*, 2010, **39**, 1562–1581.

51 J. G. Christensen, J. Burrows and R. Salgia, *Cancer Lett.*, 2005, **225**, 1–26.

52 A. Danilkovitch-Miagkova and B. Zbar, *J. Clin. Invest.*, 2002, **109**, 863–867.

53 X. Liu, R. C. Newton and P. A. Scherle, *Trends Mol. Med.*, 2010, **16**, 37–45.

54 J. P. Eder, G. F. Vande Woude, S. A. Boerner and P. M. LoRusso, *Clin. Cancer Res.*, 2009, **15**, 2207–2214.

55 J. Eberhardt, D. Santos-Martins, A. F. Tillack and S. Forli, *J. Chem. Inf. Model.*, 2021, **61**, 3891–3898.

56 S. Rampogu, B. Shaik, J. H. Kim, T. S. Jung, M. W. Ha and K. W. Lee, *Heliyon*, 2023, **9**, e13324.

57 S. Rampogu, T. S. Jung, M. W. Ha and K. W. Lee, *Sci. Rep.*, 2023, **13**, 10583.

58 N. T. T. Chi, V. T. Pham and H. V. Huynh, *Organometallics*, 2020, **39**, 3505–3513.

59 J. H. Park, Y. Liu, M. A. Lemmon and R. Radhakrishnan, *Biochem. J.*, 2012, **448**, 417–423.

60 S. Eathiraj, R. Palma, E. Volckova, M. Hirschi, D. S. France, M. A. Ashwell and T. C. K. Chan, *J. Biol. Chem.*, 2011, **286**, 20666–20676.

61 W. L. DeLano, *CCP4 Newsletter on Protein Crystallography*, 2002, vol. 40, pp. 82–92.

62 O. Trott and A. J. Olson, *J. Comput. Chem.*, 2010, **31**, 455–461.

63 D. Van Der Spoel, E. Lindahl, B. Hess, G. Groenhof, A. E. Mark and H. J. C. Berendsen, *J. Comput. Chem.*, 2005, **26**, 1701–1718.

64 V. Zoete, M. A. Cuendet, A. Grosdidier and O. Michielin, *J. Comput. Chem.*, 2011, **32**, 2359–2368.

65 D. J. Price and C. L. Brooks III, *J. Chem. Phys.*, 2004, **121**, 10096–10103.